www.springer.com/41230
https://doi.org/10.1007/s41230-026-4277-4



# Numerical simulation and experimental verification of filling, solidification, and warpage for large scale integrated aluminum alloy high-pressure die casting parts

**Xiao-ying Ma[1], Yu-ling Lang[1], Ming-lei Li[1], Shi-wen Xu[1], Jia-xin Hou[1], Hai-ping Chang[1], Hai-feng Liu[1], Ya-chun Wan[1], Xing-fu Liu[1], *Peng-ji Xue[2], Shi-qi He[2, 3], Hao Shi[2, 3], Xiang-qian Ma[1], Yu-gang Gao[1], and Yi-ge Peng[1]**

*1. CITIC Dicastal Co., Ltd., Qin Huangdao 066011, Hebei, China*

*2. Beijing Supreium Co., Ltd., Beijing 100083, China*

*3. Suzhou Supreium Technology Co., Ltd., Suzhou 215200, Jiangsu, China*

Copyright © 2026 Foundry Journal Agency

**Abstract:** Lightweight is the trend of automotive development, and integrated die casting provides a low-cost and efficient implementation path for lightweight. Due to the overall size of integrated die castings being much larger than traditional die castings, existing die casting data and experience are difficult to apply to the production of integrated die castings, and computer simulation is needed to assist in design and production. In this study, a new mathematical model of fluid flow, heat transfer, and thermal-stress coupling in the entire die-casting process was established on the SupreCAST platform and the filling, solidification, and warping deformation of large scale integrated Al-Mg-Si die-casting products were simulated based on the Lattice Boltzmann method and thermal-stress coupling model, taking the high Reynolds number turbulent two-phase flow, unsteady interfacial heat transfer coefficient, and nonlinear material constitutive relationship into account. By analyzing the flow pattern, the air entrainment at the filling end of the integrated die casting was predicted. Deformation analysis was conducted on the full die casting process of the integrated frame, and the warpage of the parts was predicted. An shrinkage deformation in *X*- and *Y*-direction is about 0.8 mm and 1.4 mm, respectively. In *Z*-direction, the casting has a tendency to warp upwards in the middle and downwards towards the periphery. Based on the deformation analysis, it is recommended to mitigate the warpage by homogenizing the temperature field and adding rib plates.

**Keywords:** large scale integrated high pressure die casting; warping deformation prediction; full processes; 4D interface heat transfer; filling process; solidification simulation

**CLC numbers:** TP391.9 **Document code:** A **Article ID:** 1672-6421(2026)06-815-12

## 1 Introduction

With the implementation of emission reduction goals for carbon peak and carbon neutrality, lightweighting has become a significant trend in automotive development, and integrated die casting offers a low-cost and efficient solution for achieving these goals[1, 2]. Integrated die casting involves forming multiple separate and dispersed components into a single large casting, replacing the traditional method of stamping individual components and then welding or riveting them together[3]. Compared to traditional die castings, integrated components are larger in size (1 m), requiring more materials (102 kg) and having higher overall mechanical performance requirements. Their structural design, materials selection, and processing design are beyond the scope of traditional die casting design experience. How to avoid defects and improve production efficiency during the design stage are core issues in the integrated die casting[4, 5]. With the

***Peng-ji Xue**

Male. Manager of Casting Simulation Application Engineering Department in Supreium Co., Ltd. He has led key projects including the aluminum steering knuckle and magnesium seat frame development for Hongqi H7. He received the FAW Group "Outstanding Graduate Award" in 2014.

E-mail: pj.xue@supreium.com

**Received: 2024-12-12; Revised: 2025-07-10; Accepted: 2026-03-03**

advancement of computer simulation technology, utilizing numerical simulation technology to study the die casting processing is of great significance for optimizing the integrated die casting processing design and improving the die casting quality[6, 7].

Based on existing investigations on the die casting simulation, many research groups and companies have developed the die casting simulation software, such as Flow3D from the United States[8], and MAGMA from Germany[9]. Additionally, there are specialized simulation software for various casting methods, such as ProCAST from the United States, CastCAE from Finland, Anycasting from Republic of Korea, and FTStar and Huazhu CAE from China. With the development of casting simulation technology, the above casting softwares have been utilized to guide the component, mold design, and processing optimization. Sun et al.[10] used MAGMA to simulate the casting processes of wheel hubs and studied the influence of gating system parameters on filling processes. Liu et al.[11] used AnyCasting to simulate aluminum alloy shells and determined the processing conditions with stable filling and fewer defects. Chen et al.[12] used ProCAST to simulate the filling and solidification process of frames and optimized the arrangement of ingating and overflow. The optimized ingate thickness and injection speed was 2.4 mm and 3.4 m·s$^{-1}$, respectively. Zhang et al.[13] used MAGMA to simulate shrinkage and porosity defects in the die casting process and optimized the design of the die cooling system. Chen et al.[14] used Huazhu CAE to simulate the filling and cooling processes of zinc alloy die castings and evaluated the deformation of the parts based on die surface element method. The results showed that the die surface element method successfully predicted the deformation of the casting found in the reality. He et al.[15] used ADSTEFAN to simulate the deformation and warpage of thin-walled magnesium alloy die castings and optimized the cooling water channels to reduce the deformation of the parts. Most of these softwares are deployed on personal computer or workshop with limited scalability in computational resources, leading to time-consuming for large scale simulation.

In comparison with traditional die castings, large scale integrated die castings are larger in size, with an overall size of approximately 1–2 m, and thinner in thickness (approximately 4–5 mm). To accurately reflect the flow, heat transfer, and deformation within the parts, it is necessary to discrete the thickness into multiple layers of grids, resulting in limited grid size (~1 mm) and enormous numbers of grids (~$10^8$), which greatly deteriorates computing efficiency. Moreover, the die casting process involves complex physical processes, including strong turbulent flow, complex boundary heat exchange, and thermal-mechanical coupling, which require high-fidelity mathematical models. To address these issues, the SupreCAST platform was utilized to simulate the filling, solidification, and deformation of large integrated die-casting parts during the high-pressure die-casting (HPDC) process of Al-Mg-Si alloy. The method of Lattice Boltzmann method (LBM) was used to simulate fluid flow to solve high Reynolds number turbulent two-phase flow. The whole processes of die casting were considered and the coupling model of fluid flow, heat transfer, and thermal-stress was adopted. Moreover, the SupreCAST, the first cloud-native platform for casting, offered a cost-effective and efficient solution to meet all simulation requirements for casting and die design. Then, the simulation results were compared with the experimental results to validate the accuracy of SupreCAST solver. Finally, based on the simulation results, the optimized process parameters were recommended.

# 2 Mathematical model

## 2.1 Flow model

The fluid flow in HPDC is described with Navier-Stokes equation with turbulence[16]:

$$\begin{aligned}&\frac{\partial\rho}{\partial t}+\nabla\cdot(\rho\vec{v})=0\\&\frac{\partial\rho}{\partial t}(\rho\vec{v})+\nabla\cdot(\rho\vec{v}\vec{v})=-\nabla p+\nabla\cdot((\mu+\mu t)\nabla\vec{v})+\rho\vec{g}\end{aligned}\tag{1}$$

where $\rho$ is density, $\vec{v}$ is the fluid velocity, $p$ is pressure, $\mu$ is dynamic viscosity, $\mu_t$ is turbulent viscosity, and $\vec{g}$ is gravity acceleration. The Navier-Stokes equation is solved by lattice Boltzmann method (LBM). The basic equation of LBM is as following[16]:

$$f_i(\vec{r}+\delta\vec{r},t+\delta t)=f_i(\vec{r},t)-\frac{1}{\tau}(f_i(\vec{r},t)-f_i^{\mathrm{eq}}(\vec{r},t))\tag{2}$$

where $f_i$ is the density distribution function of the particles, $f_i^{\mathrm{eq}}$ is the corresponding equilibrium distribution function, $\vec{r}$ is the spatial position vector of the particle, $t$ is the motion time of the particle at a certain time, $\delta t$ is the time step, and $\tau$ is the single relaxation time and its relationship with kinematic viscosity is[17]:

$$\tau=\frac{1}{2}+\frac{3v}{c^2\delta t}\tag{3}$$

where $c=\delta x/\delta t$ is the lattice velocity related to the grid size and time step. To describe the flow in three-dimensional space, the D3Q19 model[18] is discretized in velocity space, and the corresponding $f_i^{\mathrm{eq}}$ expression is as follows:

$$f_i^{\mathrm{eq}}=\rho w_i\left(1+\frac{3\vec{c}_i\cdot\vec{v}}{c^2}+\frac{9(\vec{c}_i\cdot\vec{v})^2}{2c^4}-\frac{3\vec{v}\cdot\vec{v}}{2c^2}\right)\tag{4}$$

where $\vec{c}_i$ is the discrete velocity along the $i$-th discrete direction of the velocity space, and $w_i$ is the corresponding weight in this direction. The large eddy simulation and volume of fluid (VOF) method are used to characterize the two-phase flow process with high Reynolds number in the die casting process[19]. In VOF method, the volume fraction $\epsilon$ of fluid and gas cells is 1 and 0, respectively. The mass exchange $\Delta M_i(\vec{r},t)$ between an interface cell at spatial position $\vec{r}$ and its neighbor in $\delta\vec{r}_i$ direction at $\vec{r}+\delta\vec{r}_i$ is calculated as:

$$\Delta M_i(\vec{r},t)=\begin{cases}0 & \vec{r}+\delta\vec{r}_i \in G\\ f_i^{\text{out}}(\vec{r}+\delta\vec{r}_i,t)-f_i^{\text{out}}(\vec{r},t) & \vec{r}+\delta\vec{r}_i \in F\\ \frac{1}{2}(\epsilon(\vec{r},t)+\epsilon(\vec{r}+\delta\vec{r}_i,t))(f_i^{\text{out}}(\vec{r}+\delta\vec{r}_i,t)-f_i^{\text{out}}(\vec{r},t)) & \vec{r}+\delta\vec{r} \in I\end{cases} \tag{5}$$

A spatial filter is applied to the velocity field, which should be fine enough that the large turbulent structures of the flow do not get filtered out. Hence, only the effect of the small sub-grid eddies on the large scale flow structures has to be modelled. This is included in the model through an additional turbulent viscosity ($v_T$). In a Smagorinsky model depends on the strain rate:

$$v_T=(C_S\Delta x)^2\left\|S_{\alpha\beta}\right\| \tag{6}$$

where $C_S$ is the Smagorinsky constant, and $S_{\alpha\beta}$ is the strain rate tensor can be computed from the moments as:

$$S_{\alpha\beta}=\frac{S_{xx}}{2\rho c^2}(\rho c^2\delta_{\alpha\beta}+\rho u_\alpha u_\beta-P_{\alpha\beta}) \tag{7}$$

where $S_{xx}$ is the viscosity, $c$ is the speed of sound, $\delta_{\alpha\beta}$ is the Kronecker symbol, $\rho$ is the density, $\mu$ is the velocity, and $P_{\alpha\beta}$ is the second-order moments of the distribution functions. From Eq. (3), the single relaxation time ($\tau$) in LES model is shown as:

$$\tau=\frac{1}{2}+\frac{3(v_0+v_T)}{c^2\delta t} \tag{8}$$

## 2.2 Heat transfer model

The temperature field during the metal solidification process can be described by the heat transfer equation with a heat source term[20]:

$$\frac{\partial}{\partial t}(\rho c_p T)+\nabla\cdot(\rho c_p\vec{v}T)=\lambda\nabla^2T+\rho L\frac{\partial g_s}{\partial t} \tag{9}$$

where $T$ represents temperature, $c_p$ represents specific heat capacity, $\lambda$ represents thermal conductivity, and $L$ represents the latent heat during solidification. The solid fraction ($g_s$) is assumed to decrease linearly as the temperature decreases[21]:

$$g_s=\frac{T_l-T}{T_l-T_s} \tag{10}$$

where $T_l$ and $T_s$ refer to the liquidus and solidus lines, respectively. For boundary conditions, the four-dimensional (4D) interfacial heat transfer coefficient (IHTC) calculated by the interface inverse method is used to represent the equivalent convective heat transfer coefficient of the casting boundary during die casting[22, 23]. Due to the complex phenomena in HPDC including flow, solidification, and interface pressure, the IHTC changes dramatically over time and the 4D denotes the four dimentions in which the heat transfer coefficient varies not only in the traditional three-dimensional (3D) spatial dimensions ($x$, $y$, $z$) but also in time dimension ($t$). The 4D interfacial heat transfer coefficients in HPDC can be divided into four stages, namely the initial increasing stage, the high value maintaining stage, the fast decreasing stage, and the low value maintaining stage. During the fast decreasing stage, the IHTC ($h$) changes as a function of the solid fraction ($f_s$):

$$h=h_0+k_{h-f}(1-f_s)^{\varepsilon} \tag{11}$$

where $k_{h\text{-}f}$ and $\varepsilon$ are fitting parameters based on experimental data, $h_0$ is the IHTC after complete solidification. The initial die surface temperature ($T_{DI}$) has the dominant influence on the IHTC peak value ($h_{max}$) and through correlation analysis, the following relationship is found to have the best description:

$$h_{max}=\exp(\gamma_h)T_{DI}^{2+\beta_h} \tag{12}$$

where $\gamma_h$ and $\beta_h$ are the fitting parameters based on experimental data. The convection heat transfer coefficient is determined by the following equation:

$$h=0.8418(T_{surf}-T_w)^{1/3} \tag{13}$$

where $T_w$ represents environment temperature and $T_{surf}$ is the casting's surface temperature.

## 2.3 Stress-strain model

During the casting process, the deformation rate of the casting is not significant, allowing the mechanical problem to be simplified into a quasi-static analysis, where the inertial and viscous terms are neglected[24]. The equilibrium equation is as follows[25]:

$$\nabla\cdot(D_{ijkl}\varepsilon_{kl}^e)=0 \tag{14}$$

where $D_{ijkl}$ represents the elastic modulus tensor, and $\varepsilon_{kl}^e$ represents the elastic deformation. During the casting process, the total strain comprises three components:

$$\varepsilon_{ij}=\varepsilon_{ij}^e+\varepsilon_{ij}^p+\varepsilon_{ij}^{th} \tag{15}$$

where $\varepsilon_{ij}$ is the total strain, $\varepsilon_{ij}^p$ is the plastic strain, and $\varepsilon_{ij}^{th}$ is the thermal strain. For thermal strain, the thermal expansion coefficient $\alpha_T$ is used to describe $\varepsilon_{ij}^{th}$:

$$\varepsilon_{ij}^{th}=\alpha_T(T-T_{ref})\delta_{ij} \tag{16}$$

where $T$ is the temperature calculated by casting solidification simulation, $T_{ref}$ is the reference temperature, $\delta_{ij}$ is Kronecker symbol.

For metallic polycrystalline materials, the nonlinear stress-strain relationship of the material is represented by an ideal elastoplastic body with temperature-dependent properties[26]. The von-Mises yield criterion is used to determine whether an element enters a plastic state, and the associated plastic deformation relationship is[27]:

$$\mathrm{d}\varepsilon_{ij}^p=\frac{\partial f}{\partial\sigma_{ij}}\mathrm{d}\lambda \tag{17}$$

where $f$ is the yield function, and it follows the laws of elasticity during unloading. For boundary conditions, the die surface is assumed to be a smooth and rigid contact surface, and a point-to-surface contact model is used to handle the contact between the part and the die during in-die cooling[28]. After ejection, the part is in a free and unconstrained state[29].

### 2.4 Calculation strategy

The entire process of die casting is divided into multiple time steps for calculation. In each time steps, the fluid flow is solved by the LBM method firstly and the velocity and pressure fields are obtained. Then, the temperature field is solved by the finite volume method and the convection term is calculated based on the obtained velocity. Next, the stress-strain equation is solved by the finite element method, and the contact problem between the die and the part is solved by the Lagrange multiplier method. In the calculation of stress deformation, the influence of the flow in filling process on the stress deformation is ignored, and the shrinkage is calculated based on the temperature field solved before.

## 3 Results and discussion

### 3.1 Geometry model

Figure 1 shows a three-dimensional model of the part analyzed in this study, which is a large scale integrated Al-Mg-Si alloy casting. The dimensions of the part are 1.4 m in length, 1.3 m in width, and 0.5 m in height, with an average wall thickness of 5 mm.

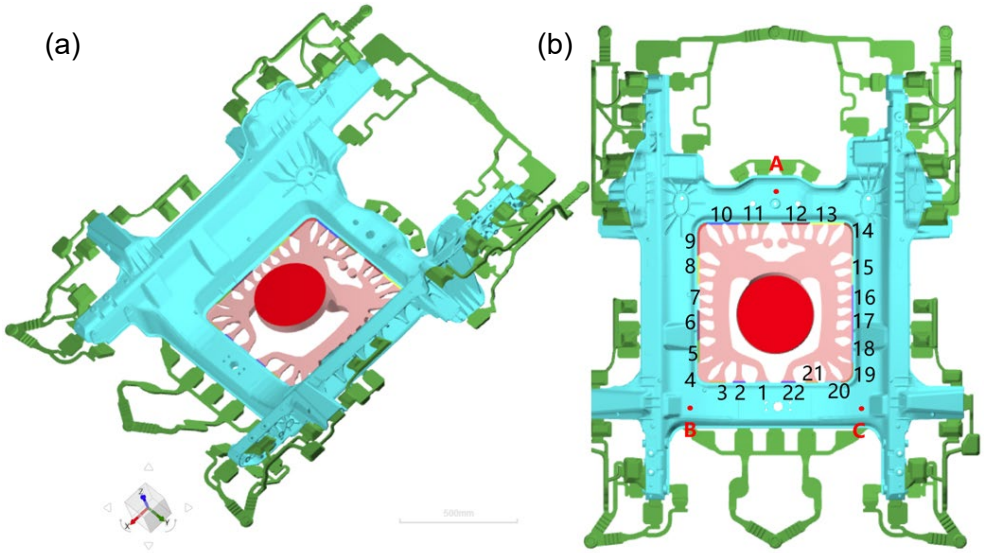



**Fig. 1: Part model and markings: (a) three-dimensional model of the part; (b) top view of the part, gating system numbering, and reference points (A, B, C) for stress calculation constraints**

The present Al-Mg-Si alloy can achieve a yield strength of 160–180 MPa, tensile strength of 300–320 MPa, and elongation of 15%–20% without heat treatment[30]. Due to its excellent characteristics, this Al-Mg-Si alloy is mainly used for chassis parts, meeting the requirements of high impact and fatigue durability. The physical properties of the Al-Mg-Si alloy calculated by the material supplier using Jmatpro are shown in Fig. 2. These properties data can be simply imported into the SupreCAST software for use. The casting weight was nearly 100 kg, and it was formed by an 8800 T gigacasting machine. The die casting process adopted multi-stage speed technology, and the specific velocity curve is shown in Fig. 3. The initial die temperature was set to 180 °C and pouring temperature was set to 670 °C.

The SupreCAST platform was utilized to analyze the filling, solidification, and warpage of large scale integrated Al-Mg-Si alloy parts during the die casting process. During the filling and solidification process, the mesh size was set to 1 mm for fluid flow and temperature calculation with a total of approximately 250 million filling grids and 330 million solidification grids. For warping deformation analysis, 40.84 million tetrahedral grids were used for calculation. The size of the tetrahedral grids was determined using curvature-adaptive mesh refinement technology, with larger grids on flat surfaces and finer grids on curved surfaces based on the curvature size, ensuring that the geometric error is less than 0.5 mm. In stress calculation, constraints need to be added to the model to obtain a unique solution. The constraints for this part are shown in Fig. 1(b), where Point A restricts the freedom of movement in three directions, i.e., the displacement is 0; Point B restricts the freedom of movement in two directions, and can only move along the line formed by AB; Point C restricts the freedom of movement in one direction, and can only move on the plane determined by Points A, B, and C. A total of 6 degrees of freedom are constrained, and a unique solution can be obtained for mechanical calculations in three-dimensional space.

### 3.2 Flow analysis results

The molten metal is poured from the holding furnace into the die casting machine barrel and enters the injection stage to start the die casting process. The relationship between the plunger position and velocity is shown in Fig. 3. As shown in Fig. 3, the entire filling process is divided into four stages: slow advancement stage, acceleration stage, high-speed filling stage, and deceleration stage. The slow advancement stage is the initial filling stage, during which the molten metal mainly flows in the barrel, corresponding to the area between Points 1 and 5 in Fig. 3. The acceleration stage is a transition period from slow to high-speed advancement of the plunger,

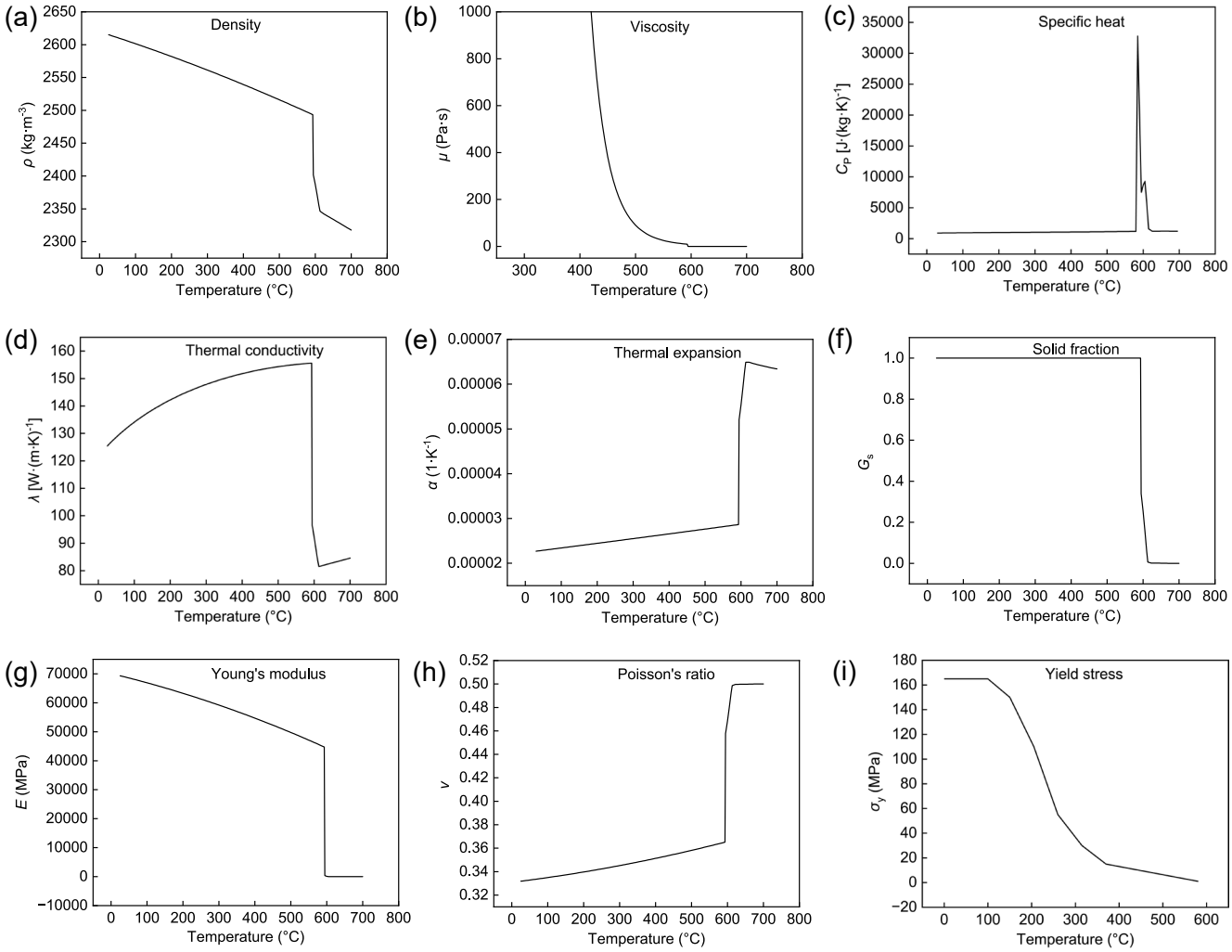



**Fig. 2: Physical property of Al-Mg-Si, including density $\rho$ (a), viscosity $\mu$ (b), specific heat $C_p$ (c), thermal conductivity $\lambda$ (d), thermal expansion $\alpha$ (e), solidification path $G_s$ (f), elastic modulus $E$ (g), Poisson's ratio $\nu$ (h), and yield stress $\sigma_y$ (i)**

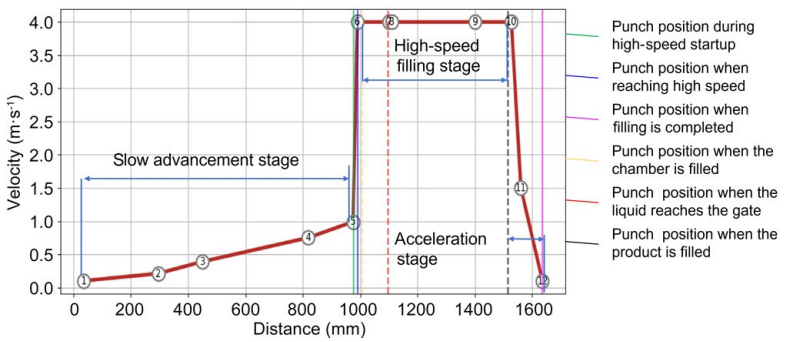



**Fig. 3: Velocity-distance curve for multi-stage injection process**

corresponding to the area between Points 5 and 6 in Fig. 3. The high-speed filling stage is the stage of filling the die casting part, corresponding to the period between Points 6 and 10 in Fig. 3. The deceleration stage is the period when the plunger transitions from high to low speed before the part is completely filled, corresponding to the period between Points 10 and 12 in Fig. 3.

The flow conditions during the slow advancement stage and the high-speed filling stage are illustrated in Fig. 4. Figure 4(a) shows the flow of molten metal within the barrel when the punch initially begins to move. At this point, the flow velocity in most regions of the molten metal is 0, with only the metal close to the punch moving due to its motion. The initial punch velocity is 0.1 m·s$^{-1}$, and the maximum fluid velocity is 0.33 m·s$^{-1}$, primarily attributed to the wave-like motion of the molten metal. As the punch advances, the level of molten metal within the barrel gradually rises, as depicted in Figs. 4(b)–(c). The punch velocity gradually increases from 0.1 m·s$^{-1}$ to 0.33 m·s$^{-1}$ and then to 0.48 m·s$^{-1}$, with corresponding maximum flow velocities of 0.45 m·s$^{-1}$ and 0.67 m·s$^{-1}$, respectively. When the punch reaches the time Point 4 in Fig. 3, the barrel is almost filled, as shown in Fig. 4(d). At this moment, the punch velocity is 0.75 m·s$^{-1}$, and the maximum local flow velocity of the molten metal reaches 8.73 m·s$^{-1}$, which indicates that gas is gradually being expelled from the barrel without entering the liquid metal to form bubbles. When the punch position reaches the time Point 5 in Fig. 3, high-speed motion starts, and the punch velocity reaches 1.39 m·s$^{-1}$. The molten metal has already entered the runner from the barrel, as illustrated in Fig. 4(e). Due to the significantly smaller cross-sectional area of the runner compared to the barrel, the maximum

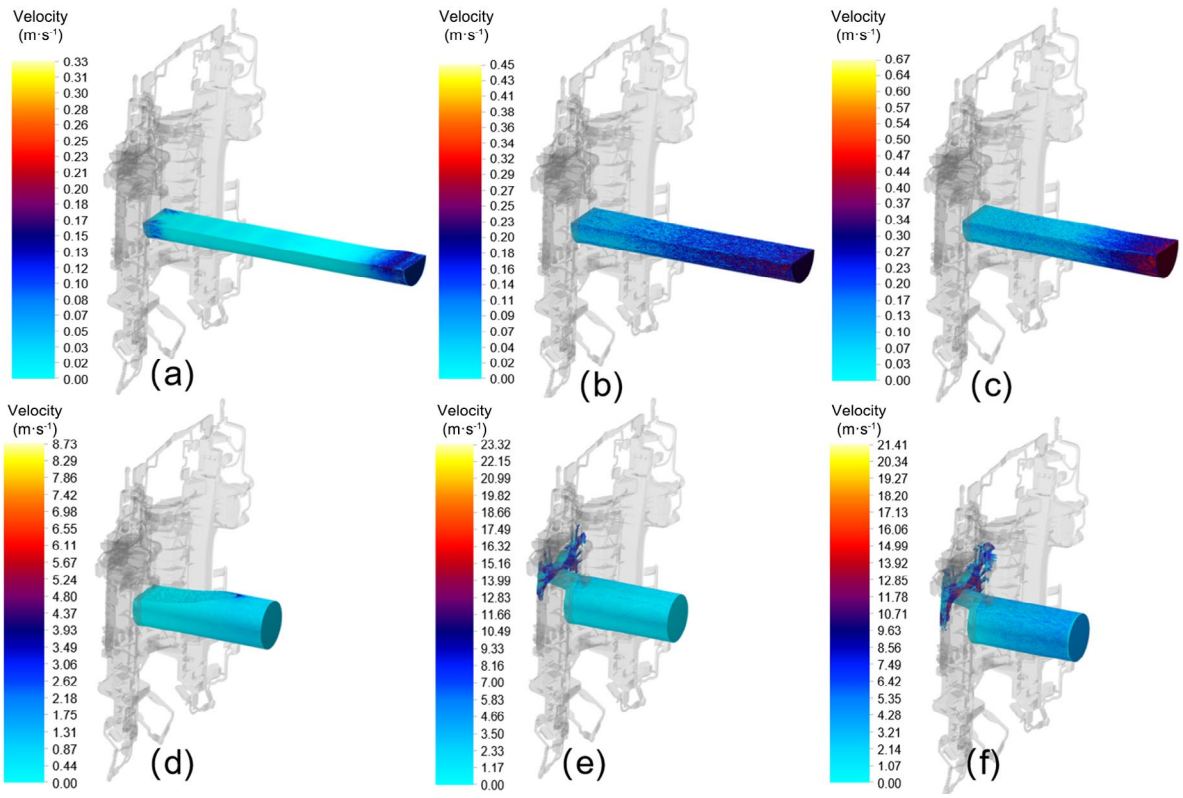



**Fig. 4: Two-phase interface and velocity contour in the barrel, (a)–(f) correspond to the time points 1–6 in Fig. 3, respectively**

local velocity increases to 23.32 m·s$^{-1}$. Upon completion of the high-speed motion, the punch velocity reaches 4 m·s$^{-1}$, further propelling the liquid metal into the runner, while a small amount of molten metal enters the part cavity through the gate, as shown in Fig. 4(f). When observing the flow state within the barrel, the molten metal remains stable without apparent gas entrainment throughout the punch motion.

The filling process of aluminum alloy parts is shown in Fig. 5. Figure 5(a) depicts the state of metal liquid filling at the initial high-speed moment. The liquid metal in the runner preferentially enters the part through the ingates located on the upper left and upper right, while the runner below remains partially unfilled. When the filling reaches 21.96%, the entire runner is filled with liquid metal, and the liquid metal begins to enter the part through the bottom ingate, as shown in Fig. 5(b). At this stage, most of the liquid metal passing through the ingates exhibits a noticeable jetting phenomenon, with distinct sharp flow fronts visible ahead of the ingates. As the filling progresses, the liquid metal firstly fills the beams connected to the ingates, as depicted in Fig. 5(c), where the jetting phenomenon in front of the ingates is still evident. The filling continues to 56.91%, as shown in Fig. 5(d), where the beams connected to the ingates are completely filled, and the slag traps below are also full. The next step involves filling the four corners of the part. When the filling reaches 79.98%, the main body of the lower half of the part is essentially full, with the remaining distal portion of the upper half and the unfilled slag traps, as shown in Fig. 5(e). Due to the convergence of the primary liquid flow towards the four corners, there are two local maximum velocity points observed on the beams on both sides of the center. This is primarily attributed to the localized velocity concentration zones that arise during the process of metal entering from nearby ingates and converging towards the four corners. Figure 5(f) shows the flow state just before the completion of filling, where the filling volume is approximately 99.16%. At this point, the punch speed decreases, and the maximum flow velocity within the casting drops from 40 m·s$^{-1}$ to 28 m·s$^{-1}$, with only a local maximum velocity present in the exhaust wave plate area of the final filling region.

The die casting experiments were conducted at CITIC Dicastal and the experimental parameters were performed according to Section 3.1. Corresponding defect identification was analyzed. Figure 6 presents a schematic diagram predicting entrapped air defects and experimental result is shown in Fig. 6(c). Figure 6(a) displays the morphology of the flow front when the overall filling reaches 69.62%, where the flow front is actively filling the ears on both sides of the die. Figure 6(b) is an enlarged view of the flow front at the ears, revealing that the liquid from both sides converges towards the center, which makes it susceptible to entrap the gas in the middle and then incorporate it into the final part. Additionally, the head-on collision of fluids from both sides often leads to chaotic flow. The final casting part, as shown in Fig. 6(c), exhibits significant defects at the ears. It is recommended to install a slag trap at the top to mitigate the tendency of encapsulating gas in this region. Concurrently, increasing the mold temperature around this area can enhance the fluidity of the molten metal during filling, thereby improving gas and slag evacuation capabilities.

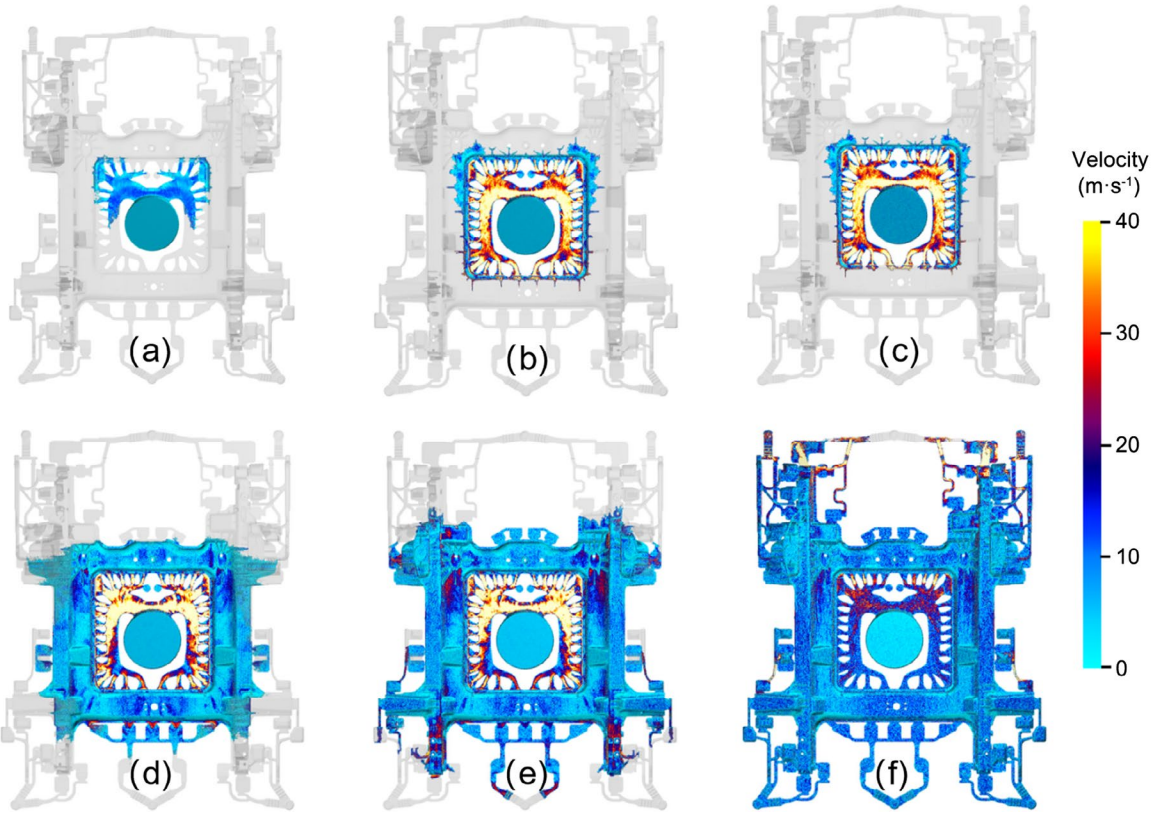



**Fig. 5: Filling process of aluminum alloy part, with the corresponding filling percentages indicated as follows: (a) 14.31%; (b) 21.96%; (c) 33.08%; (d) 56.91%; (e) 79.98%; (f) 99.16%**

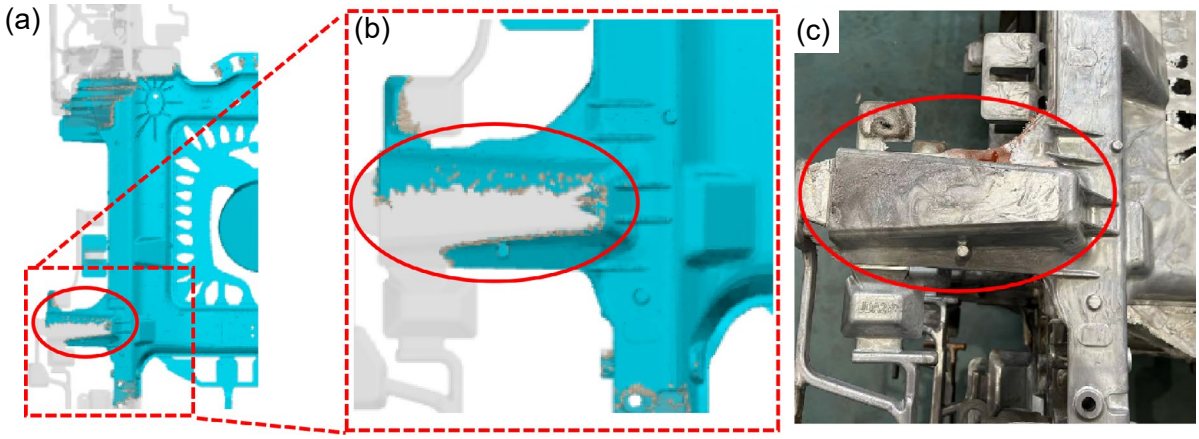



**Fig. 6: Prediction of entrapped air process: (a) filling to 69.62%; (b) schematic diagram of flow front at the ears on both sides; (c) on-site photograph**

### 3.3 Analysis of temperature results

The temperature variations of the liquid metal during the filling process are shown in Fig. 7. The temperature continuously decreases as the filling process progresses. When the filling volume reaches 33%, the temperature at the top crossbeam drops from the initial 710 °C to 700 °C, while the temperature at the bottom crossbeam decreases to 690 °C, which is 10 °C lower than that at the upper crossbeam, as depicted in Fig. 7(a). When the filling reaches 66%, the temperature of the liquid metal at the upper crossbeam drops to 697 °C, and that at the lower crossbeam decreases to 688 °C, as shown in Fig. 7(b). By the end of the filling process, the lowest temperature at the lower crossbeam position is 660 °C, while that at the upper cross-beam is 678 °C, and the lowest temperature at the positions of the two side slides is 650 °C, as indicated in Fig. 7(c). Since the influence of die temperature and water cooling on the part is neglected, the actual filling temperature may be lower. Therefore, attention should be paid to the accumulation of cold material in these areas. Additionally, the wall thickness and the temperature differences of the part affect the final warping deformation, which highlights the importance of considering the change in casting temperature when performing warping deformation analysis.

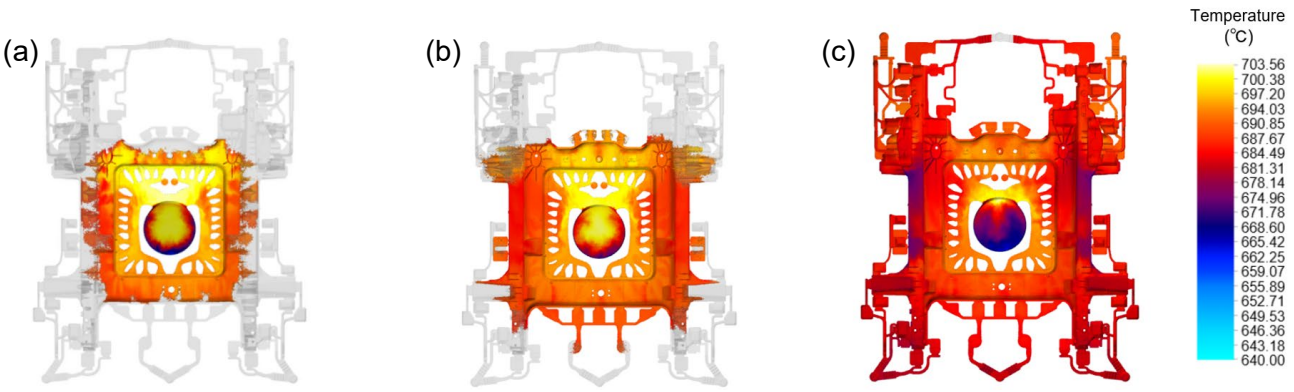



**Fig. 7: Temperature distribution at different stages during filling: (a) 33% filling; (b) 66% filling; (c) 99% filling**

After the filling is completed, the casting needs to stay in the die for a certain period of time to continue cooling. The die can be opened and the casting can be taken out only when the liquid metal is completely solidified and the casting has a certain strength. At this time, the temperature at the four corners of the casting is relatively high, about 400 °C, while the temperature of the crossbeams on both sides is lower, about 230 °C, with a temperature difference of nearly 170 °C between these two parts, as shown in Fig. 8. This is mainly because the structure of the four corner areas of the product is more complex than that of the crossbeams on both sides. There are more intersecting reinforcing ribs in the four corners, which leads to a significant increase in the wall thickness of these parts. As a result, the energy of the molten metal tends to accumulate here, prolonging the solidification time of the molten metal, and ultimately causing a large temperature difference between different parts of the casting at the same time.

## 3.4 Analysis of deformation and stress results

The calculation of deformation and stress begins when the metal fills the die cavity, encompassing the entire process of die casting, including in-die cooling, ejection, and post-die cooling. During in-die cooling, the temperature-dependent elastoplastic model and the contact between the die and part are considered. The ejection process calculates the deformation that occurs as the part is separated from the die. Post-die cooling involves calculating the deformation of the part as it cools in the open air outside the die. When in contact with the die, the die surface is smooth, and the interaction with the part consists only of pressure perpendicular to the die surface, without any friction along the die surface.

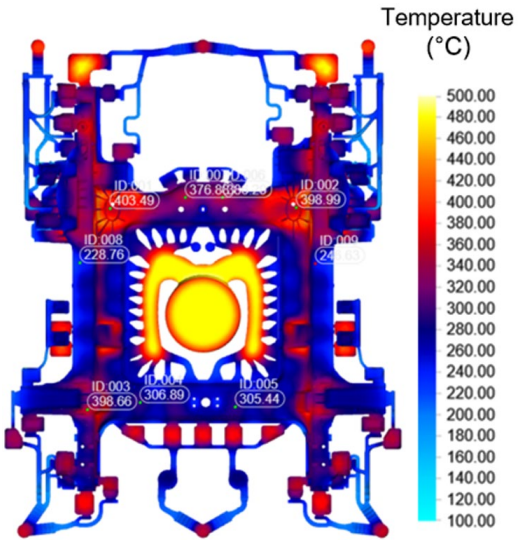



**Fig. 8: Distribution of overall temperature of the part at the time of mold opening**

Figure 9 presents the deformation distribution of the part before die opening, after ejection, and during air cooling at room temperature, with deformation represented by the magnitude of the displacement field. The physical implication of displacement represents the magnitude of positional offset of points on the part relative to their initial state. Figure 9(a) shows the deformation distribution of the part inside the die before die opening, where the part is sufficiently cooled and is ready to be extracted from the die. Due to the constraints of the die, the displacement of the part is relatively small, with most locations experiencing displacements less than 0.1 mm. Only a few areas, such as slag pockets and overflow channels, can freely shrink, resulting in larger displacements caused by shrinkage ranging from 0.1 to 0.5 mm. The maximum displacement occurs at the end slag pocket, measuring 0.51 mm.

The deformation distribution of the part after ejection is shown in Fig. 9(b). Compared to that before die opening, the part after ejection is no longer constrained by the die, allowing stress release and subsequent deformation. Since the die surface is assumed to be absolutely smooth, deformation due to forces during ejection is negligible, and thus, the analysis of part deformation caused by ejector pins is omitted. The maximum deformation of the part after ejection is 4.6 mm, occurring at the slag pocket farthest from the constraint Point A, as shown in Fig. 1(b). Since the deformation of the part arises from thermal contraction, the magnitude of displacement is positively correlated with the distance from the constraint point, indicating a uniform shrinkage around the constraint point.

The deformation result after complete cooling to room temperature in Fig. 9(c) exhibits a similar overall distribution pattern to that after ejection, both positively correlated with the distance from the constraint point. As the temperature further decreases, the part continues to shrink, leading to an increase in the displacement of points on the part, with a maximum value of approximately 10 mm.

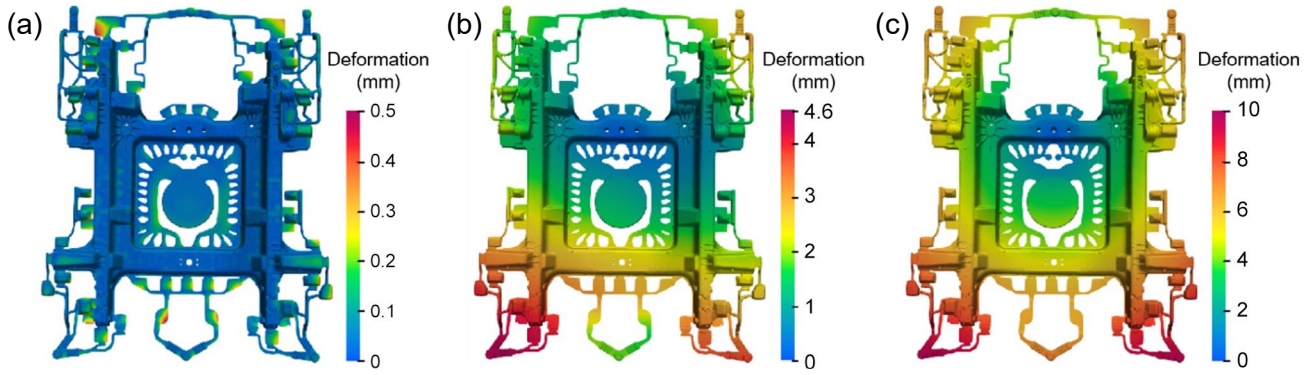



**Fig. 9: Deformation distribution of the part at different stages: (a) before mold opening; (b) after ejection; (c) cooled to room temperature**

The stress distribution at three stages during the die casting process is shown in Fig. 10, with the von-Mises equivalent stress used to describe the stress state of the casting. Before die opening, the part cools and shrinks within the die. Due to the constraints of the die, the part cannot shrink freely, resulting in significant stress within the die. Most regions reach the yield limit and enter a state of plastic deformation, as shown in Fig. 10(a). The maximum stress is 100 MPa, determined by the yield strength of the material. During die opening, the temperatures for most regions of the part are between 150–200 °C, with a yield strength of approximately 100 MPa. Once the part leaves the die, the die constraints are removed, and the internal stress within the part is released, causing the von-Mises equivalent stress to drop rapidly, as illustrated in Fig. 10(b). Due to the uneven temperature distribution across the casting component, resulting in uneven shrinkage and deformation, there still exists residual stress without die constraints and the maximum stress value on the casting component is approximately around 40 MPa. After ejection, the part further cools to room temperature in the air, undergoing further shrinkage. Without external constraints, the overall stress distribution of the part changes insignificantly, with the maximum stress occurring at the sharp corners near the runner, reaching 200 MPa.

In structural mechanics calculations, deformation results are typically dependent on the choice of reference configuration. In this study, the die cavity is seleted as the reference configuration and corresponding results are shown in Fig. 9. However, in practical die design, the deformation results related to the target die as the reference configuration are more important. In die design, shrinkage compensation is introduced to reduce the effect of shrinkage on the overall dimensions of the part; typically, this shrinkage compensation is uniform. In other words, the dimensions of the die cavity can be denoted as $L_{die}=(1+\delta)L_{target}$, where $\delta$ is the shrinkage rate. In the final analysis, the displacements of the part nodes relative to the die cavity need to be converted into displacements relative to the target part. This conversion requires two steps: the first step is the transformation of the reference origin, converting the reference point of the displacement field to a fixed reference point. In this study, the reference point is chosen as Point A in Fig. 1(b), with the transformation expressed as follows:

$$\begin{aligned} D&=D_{origin}-D_A \\ P&=P_{origin}-P_A \end{aligned} \tag{18}$$

where $D_{origin}$ and $P_{origin}$ represent the original displacement field data and node positions, respectively, $D_A$ and $P_A$ represent the displacement and node position data for Point A. The transformation converts the displacement field to a new diplacement field refered to Point A. The second step involves incorporating the shrinkage amount into the actual displacement field. Since the shrinkage is uniform, the following formula is used to modify the displacement field:

$$D_{transform}=D+\delta\cdot P \tag{19}$$

where $\delta$ represents the displacement relative to the target part point after transformation, $P$ and $D$ are the coordinates

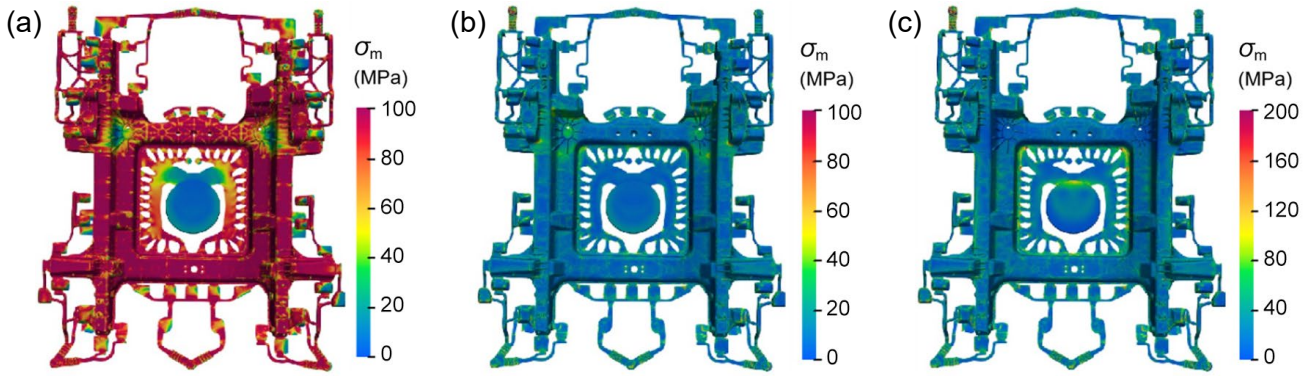



**Fig. 10: von-Mises equivalent stress distribution of the part at different stages: (a) before mold opening; (b) after ejection; (c) air-cooled to room temperature**

and displacement of the node after the reference frame transformation. We assume that the recommended shrinkage rate should be selected to minimize the deformation:

Find rigid body transformation to minimize $\Sigma\left\|D_{\text{transform}}\right\|^2$.

Then, the shrinkage rate expression is recommended:

$$\delta = \frac{-\Sigma D \cdot P}{\Sigma P \cdot P} \tag{20}$$

For the casting in this study, the shrinkage is equal to 7‰ based on the expression above.

A contour plot of the displacement *X*-component ($D_x$) after considering shrinkage is shown in Fig. 11(a), where the gray transparent part represents the original position of the target part, and the colored part represents the position of the part after deformation. The maximum and minimum displacement values in the *X*-direction are obtained on the slag inclusion and the overflow channel, respectively, which is mainly due to the torsion generated at the connecting regions between the overflow channel and the part and/or between the slag inclusion and the part. Since the slag inclusion, runner, and overflow channel will be removed in the later stages, i.e., not appearing as final products in actual application scenarios, the deformation of these parts can be ignored. The maximum and minimum displacement values in the *X*-direction are 0.34 mm and –0.60 mm, respectively, located at the two ends of the part in the *X*-direction. Besides, the value of $D_x$ decreases monotonically along the positive *X*-direction and it is relatively uniform along the *Y*-direction. This distribution is consistent with the displacement distribution of uniform shrinkage, indicating that there is some residual shrinkage deformation in the *X*-direction of the part, but there is no obvious trend of warpage.

The contour plot of the *Y*-component displacement ($D_y$) after considering shrinkage is shown in Fig. 11(b). The maximum and minimum values of the *Y*-direction displacement are 0.61 mm and –0.61 mm, respectively, located at the two ends of Section A of the part in the *Y*-direction. At Section A, the left side of the part shifts towards the positive *Y*-direction, while the right side shifts towards the negative *Y*-direction, indicating an overall inward tendency of the part. In contrast, at the lower section B, the *Y*-direction displacement of the entire section ranges between 0 and 0.2 mm, which can be negligible compared to Section A. Due to the difference in the *Y*-direction displacement between Sections A and B, the entire part exhibits an inward trend along the arrow at Section A, resulting in a deviation of 0.7 mm. Additionally, the left and right meshes are not perfectly symmetrical during mesh generation, which leads to the asymmetry between the left and right sides.

The contour plot of the *Z*-component displacement ($D_z$) after considering shrinkage is presented in Fig. 11(c). The *Z*-direction displacement component exhibits a characteristic distribution of being higher in the center and lower towards the periphery of the part. The deformation trend is illustrated in the left-side view of the part. The maximum *Z*-direction displacement offset occurs at the four corners of the part, with a maximum offset of approximately 1 mm.

The distribution of displacement components along the *X*-direction and *Y*-direction is shown in Figs. 12(a) and (b), respectively, where the blue curve represents the distribution of the *X*-direction displacement component. The *X*-component of displacement decreases monotonically with the increase in the *X*-coordinate, and the coordinate of the intersection point with the $y$=0 line is close to the *X*-coordinate of reference Point A. In the *Y*-direction distribution, the variation in the *X*-component of displacement is less than 0.2 mm, indicating that the *X*-direction displacement component is dominant due to uniform shrinkage of the part. An increase in the shrinkage rate by 0.4‰ can be considered to eliminate the dimensional deviation in the *X*-direction. The *Y*-component of displacement is represented by the yellow curve. The *Y*-displacement distribution along the *X*-direction first increases and then decreases, with a difference of 0.6 mm between the maximum and minimum values. This indicates that the *Y*-direction displacement component is non-monotonic along the *X*-direction, which can cause warping deformation of the part. In contrast, the distribution of the *Y*-component of displacement along the *Y*-direction is nearly linearly decreasing, suggesting an inward shrinkage deformation trend with a total shrinkage of 1.4 mm. The *Z*-direction displacement component exhibits a trend of first increasing and then decreasing in both *X*-direction and *Y*-direction, indicating that the part has a tendency to warp upwards in the middle and warp downwards towards the periphery.

In die casting process, the deformation primarily originates

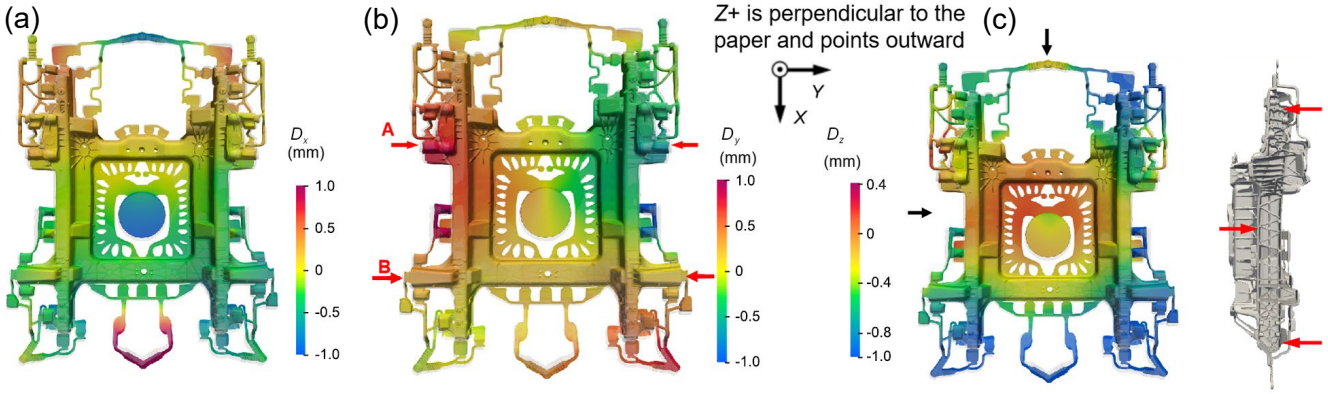



**Fig. 11: Contour plots of displacement in the *X*-direction (a), *Y*-direction (b), and *Z*-direction (c) of the part when considering shrinkage**

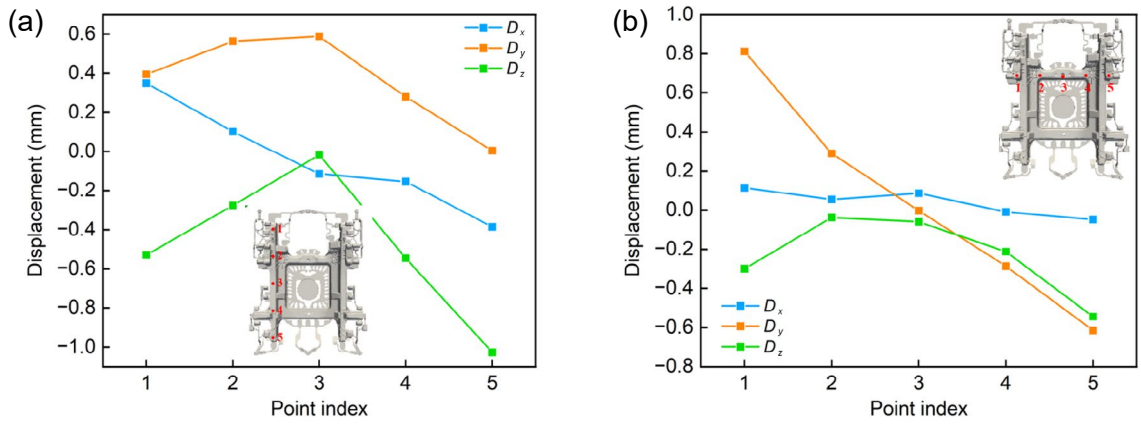



**Fig. 12: Distribution of displacement components along different paths: (a) *X*-direction; (b) *Y*-direction**

from thermal shrinkage, which is related to the temperature distribution of the casting. Therefore, the mechanisms of deformation can be investigated through analysis and control of the temperature field, thereby enabling optimization of casting distortion. According to the temperature distribution during die opening (Fig. 8), two localized high-temperature areas (ID001 and ID002) can be seen at Section A. Due to the local high temperature, the part experiences significant shrinkage after cooling outside the die, leading to an inward deformation at these locations. It is recommended to enhance heat exchange in the die at these areas to reduce the warping and deformation caused by these hot spots.

## 4 Conclusions

This work solves a coupled model for die filling flow, solidification heat transfer, and thermal stress during die casting. This model is applied to the simulation of the die casting process of integrated casting parts, enabling the prediction of defects such as flow marks, trapped gases, and deformation during the die casting of large scale integrated parts. The main conclusions are as follows:

(1) Filling simulation reveals the flow patterns within the barrel, runner, and casting during cavity filling. The filling sequence and the flow rate of each ingate are determined, and the trapped gas defects at the filling end are predicted. At the end of filling, the simulation predicts the occurrence of air entrapment defects on both sides of the die. Furthermore, when compared with experimental results, the simulation results show excellent agreement. It is recommended to alter the flow pattern by modifying the slag trap, thereby mitigating the trapped gas defects at that location.

(2) By coupling the flow field and the temperature field, the temperature distribution during the filling process and the cooling and solidification process are obtained, revealing the temperature field and hot spot distribution on the casting. The temperature at the four corners of the casting is 170 °C higher than that in the crossbeams, forming hot spots that include shrinkage porosity.

(3) Deformation analysis reveals that under the current process, the casting exhibits warpage with a magnitude of 1.4 mm and 1 mm in the *Y* and *Z* directions, respectively. This type of deformation can be mitigated by methods such as homogenizing the temperature field and adding reinforcing ribs.

## Conflict of interest

The authors declare that they have no known competing financial interests or personal relationships that could have appeared to influence the work reported in this paper.

## References

[1] Zhan H Y, Zeng G, Wang Q, et al. Unified casting (UniCast) aluminum alloy – A sustainable and low-carbon materials solution for vehicle lightweighting. Journal of Materials Science & Technology, 2023, 154: 251–268.
[2] China Society of Automotive Engineers. Technology roadmap 2.0 for energy-saving and new energy vehicles. China Machine Press, 2020, 12: 539. (In Chinese)
[3] Luo A A, Sachdev A K, and Apelian D. Alloy development and process innovations for light metals casting. Journal of Materials Processing Technology, 2022, 306: 117606.
[4] Lehmhus D. Advances in metal casting technology: A review of state of the art, challenges and trends – Part I: Changing markets, changing products. Metals, 2022, 12(11): 1959.
[5] Guo Z P, Zhang W, Xue P J, et al. White paper on digital technology for integrated die-casting. Beijing Shichuang Technology Co., Ltd, 2022.8. https://supreium-static-resource.oss-cn-zhangjiakou.aliyuncs.com/official_website/backend/test/file/8fd51b98f16f37281cb7645e14adfdb0_20240403143401447.pdf. (In Chinese)
[6] Seo P K, Kim H C, and Kang C G. Numerical integration design process to develop-ment of suspension parts by semi-solid die casting process. Journal of Materials Processing Technology, 2007, 183(1): 18–32.
[7] Kang J W, Liu B L, Jing T, et al. Intelligent casting: Empowering the future foundry industry. China Foundry, 2024, 21(6): 409–426.
[8] Chen S and Zhou F. Design of gating system for radiator die castings based on FLOW-3D software. Journal of Physics: Conference Series, 2021, 2044: 012144.
[9] Fu J, Coleman J, Poole G, et al. Uncertainty propagation through a simulation of industrial high pressure die casting. Journal of Heat Transfer, 2019, 141(11): 112101.
[10] Sun Y L and Zhang Z Z. Process optimization of pouring system for die-casting aluminum alloy oil pump body. Special Casting & Nonferrous Alloys, 2015, 35(1): 37–39. (In Chinese)

[11] Hu B H, Tong K K, Niu X P, et al. Design and optimisation of runner and gating systems for the die casting of thin-walled magnesium telecommunication parts through numerical simulation. Journal of Materials Processing Technology, 2000, 105(1): 128–133.
[12] Wang C Y, Hu Q H, and Chen F. Numerical simulation and process optimization of shell seat die casting based on ProCAST. Special Casting & Nonferrous Alloys, 2019, 39(2): 143–146. (In Chinese)
[13] Shi L F, Zhao D Z, Wang P, et al. Simulation of filling process of aluminum alloy semi-solid die casting and liquid die casting. Foundry, 2012, 61(5): 494–497. (In Chinese)
[14] Chen T, Tang Y, Liao D, et al. Simulation of casting deformation based on mold surface element method. China Foundry, 2017, 14(1): 28–33.
[15] He Y, Cao W L, Zhou Z Y, et al. Numerical simulation and process comparison of thermal deformation of thin-walled magnesium alloy die castings. Hot Working Technology, 2010, 39(23): 47–49+52. (In Chinese)
[16] He X Y and Luo L S. Theory of the lattice Boltzmann method: From the Boltzmann equation to the lattice Boltzmann equation. PhysRev E, 1997, 56: 6811–6817.
[17] Qian Y H, d'Humières D, and Lallemand P. Lattice BGK models for Navier-Stokes equation. Europhysics Letters, 1992, 17(6): 479–484.
[18] Jiaung W S, Ho J R, and Kuo C P. Lattice Boltzmann method for the heat conduction problem with phase change. Numerical Heat Transfer: Part B: Fundamentals, 2001, 39(2): 167–187.
[19] Smagorinsky J. General circulation experiments with primitive equations. Monthly Weather Review, 1963, 91(3): 99–164.
[20] Voller V R and Prakash C. A fixed grid numerical modelling methodology for convection-diffusion mushy region phase-change problems. International Journal of Heat and Mass Transfer, 1987, 30(8): 1709–1719.
[21] Bellet M, Combeau H, Fautrelle Y, et al. Call for contributions to a numerical benchmark problem for 2D columnar solidification of binary alloys. International Journal of Thermal Sciences, 2009, 48(11): 2013–2016.
[22] Guo Z P, Xiong S M, Cao S X, et al. Study on the heat transfer behavior of casting/mold interface during aluminum alloy die-casting process I. Experimental study and solution of interface heat transfer coefficient. Acta Metallurgica Sinica, 2007, 43(11): 1149–1154.
[23] Guo Z P, Xiong S M, Cao S X, et al. Study on the heat transfer behavior of casting/mold interface during aluminum alloy die-casting process II. Influence of process parameters on interface heat transfer. Acta Metallurgica Sinica, 2007, 43(11): 1155–1160.
[24] Chang A and Dantzig J. Improved sand surface element for residual stress determination. Applied Mathematical Modelling, 2004, 28(6): 533–546.
[25] Zienkiewicz O C and Taylor R L. The finite element method for solid and structural mechanics. Elsevier, 2005.
[26] Wei C, Qu J, Mehr F F, et al. A thermal-stress modelling methodology in ABAQUS for fundamentally describing the die/casting interface behaviour in a cyclic permanent die casting process. Journal of Materials Research and Technology, 2021, 15(1): 5252–5264.
[27] Careglio C, Canales C, García G C, et al. A numerical study of hypoelastic and hyperelastic large strain viscoplastic Perzyna type models. Acta Mechanica, 2016, 227: 3177–3190.
[28] Kwak S Y, Hwang H Y, and Cho C. Thermal stress analysis method considering geometric effect of risers in sand mold casting process. China Foundry, 2014, 11(6): 531–536.
[29] Fackeldey M, Ludwig A, and Sahm P R. Coupled modelling of the solidification process predicting temperatures, stresses and microstructures. Computational Materials Science, 1996, 7(1–2): 194–199.
[30] Nagaumi H and Umeda T. Prediction of internal cracking in a direct-chill cast, high strength, Al-Mg-Si alloy. Journal of Light Metals, 2002, 2(3): 161–167.